Pergamon

Int. J. Heat Mass Transfer. Vol. 37, Suppl. 1, pp. 213–231, 1994

0017-9310/94 $6.00+0.00

0017-9310(93)E0060-T

The entrainment flow adjacent to an isothermal vertical surface

NEIL T. WRIGHT† and BENJAMIN GEBHART‡

† Department of Mechanical Engineering, University of Maryland, Baltimore County, MD 21228, U.S.A.; ‡ Department of Mechanical Engineering and Applied Mechanics, University of Pennsylvania, PA 19104, U.S.A.

Abstract—Results of numerical calculations of the buoyancy-induced flow adjacent to a vertical isothermal surface with a leading edge are presented. Coordinate transformations have been used to allow efficient calculation of both the boundary layer flow and the extensive ambient entrainment in-flow. A motion pressure field, which develops owing to the motion pressure deficit at the surface, drives this entrainment. Increased boundary layer mass flow results, compared with classical boundary layer theory. Conduction into the upstream entrainment region is appreciable, ahead of the leading edge. This flow, below the surface, arises as a mass sink for the distant entraining flow. Motion pressure effects determine the flow in this leading edge entrainment region and in the entrainment flow arising along such a heated surface. Modeling of both these regions is of increasing importance in many technologically important applications, such as electronics packaging.

1. INTRODUCTION

BUOYANCY-INDUCED flow adjacent to a vertical isothermal surface, with a leading edge in an extensive quiescent fluid, has been a long-studied mechanism of buoyancy-induced external flows. Figure 1 shows the geometry of such a flow. The surface is assumed to be of negligible thickness, with flow on each side. The local velocity boundary layer thickness, $\delta(x)$, is the outward distance at which the streamwise velocity, u, is 0.01 of the local maximum value. The temperature boundary layer thickness, $\delta_t(x)$, is the distance out from the surface at which the temperature excess of the fluid is 0.01 of the imposed temperature excess at the bounding surface. The flow region extends downstream and beyond the trailing edge, for a finite surface. Many previous studies have considered this kind of flow, both adjacent to a surface and far downstream of the leading edge. There the flow becomes more vigorous. The buoyancy force drives the flow. The Grashof number, Gr, increases downstream. Then, the boundary layer approximations apply with good accuracy, in this region far downstream of the leading edge. The Grashof number is the ratio of the buoyancy force to the viscous effect acting on the fluid. This may be written as

$$Gr = \left(\frac{gx^3}{\nu^2}\right)(\beta\Delta t), \qquad (1)$$

where g is the gravitational acceleration, β is the volumetric coefficient of thermal expansion, Δt is the surface temperature excess, x is the distance from the leading edge, and ν is the kinematic viscosity.

Boundary layer calculations divide the flow into two regions, a thin buoyant boundary layer immedi-

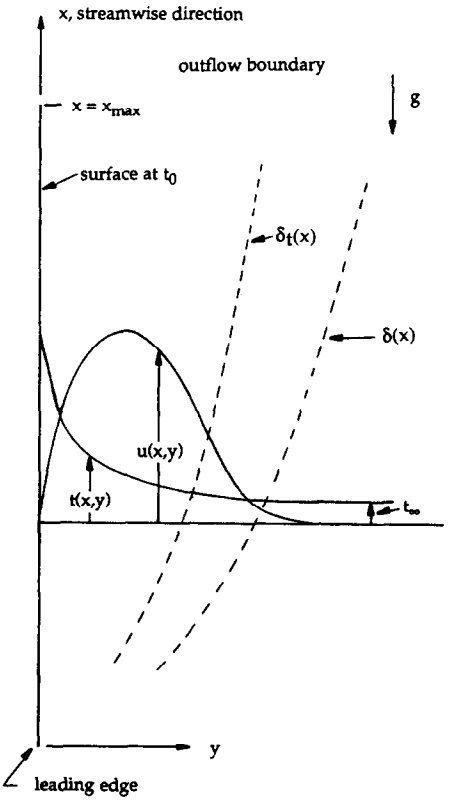

FIG. 1. Isothermal vertical surface, showing velocity and thermal boundary layers with velocity profile $u(x,y)$ and temperature profile $t(x,y)$. The horizontal scale is expanded for clarity.

NOMENCLATURE

a	constant in y-transformation, equation (18)
b	constant in x-transformation, equation (17)
c	constant in x-transformation, equation (17)
$f(\eta)$	similarity analysis streamfunction
f'	derivative of $f(\eta)$ with respect to η
g	local gravitational acceleration [m s^{-2}]
Gr	Grashof number, defined in equation (1)
Gr_{max}	Grashof number at the computational outflow boundary
k_1	constant in x-transformation, equation (17)
k_2	constant in x-transformation, equation (17)
k_3	constant in x-transformation, equation (17)
k_4	constant in y-transformation, equation (18)
$\bar{p}$	local motion pressure [kPa]
p	dimensionless motion pressure
Pr	Prandtl number, ν/α
q''	heat flux [W m^{-2}]
$\bar{t}$	local fluid temperature [°C]
$\bar{t}_\infty$	ambient fluid temperature [°C]
$\bar{t}_0$	imposed temperature of the vertical surface [°C]
$\bar{u}$	vertical velocity [m s^{-1}]
u	dimensionless vertical velocity
$\bar{v}$	horizontal velocity [m s^{-1}]
v	dimensionless horizontal velocity
x	dimensionless vertical coordinate
$\bar{x}$	dimensional vertical coordinate [m]
x'	transformed dimensionless vertical coordinate
x_{min}	minimum value of the dimensionless vertical coordinate
x_{max}	maximum value of the dimensionless vertical coordinate
y	dimensionless horizontal coordinate
$\bar{y}$	dimensional horizontal coordinate [m]
y'	transformed horizontal coordinate
y_{max}	maximum value of the dimensionless horizontal coordinate.

Greek symbols

α	thermal diffusivity [m^2 s^{-1}]
β	volumetric coefficient of thermal expansion [T^{-1}]
$\delta(x)$	similarity solution boundary layer thickness
$\delta_n(x)$	numerically calculated boundary layer thickness
δ_t	boundary layer theory temperature layer thickness
$\delta_{tn}(x)$	numerically calculated temperature layer thickness
Δt_w	$\bar{t}_0 - \bar{t}_\infty$, imposed temperature excess at surface [°C]
η	similarity analysis coordinate
ν	kinematic viscosity [m^2 s^{-1}]
$\bar{\tau}$	dimensional time [s]
τ	dimensionless time
τ_w	surface shear stress [kPa]
ϕ	temperature excess ratio
ψ	streamfunction
ω	vorticity, defined in equation (7).

ately adjacent to the surface and an outer largely inviscid distant isothermal region, throughout the rest of the fluid. The viscous forces, interacting with large temperature gradients, cause large velocity gradients in the boundary region. A streamwise velocity maximum exists within the flow. In forced flows, however, over a similar surface, the maximum streamwise velocity occurs in the freestream. Boundary layer calculations for both buoyant and forced flows commonly assume a uniform pressure level throughout the thin boundary layer and out into the ambient region. The streamwise diffusion of momentum and energy are neglected in such calculations, since these are of the order of the pressure gradients.

In the regions upstream of the leading edge and far from the surface, the buoyancy and viscous forces are both small. Far upstream, the temperature of the fluid approaches the ambient condition. In actual buoyant flows, a negative motion pressure gradient arises throughout this region. This drives the entraining flow toward the surface. This gradient results from a motion pressure deficit which arises owing to the buoyancy-driven entraining flow near the surface. The characteristics of this pressure field, and the resulting entrainment flow, are very important in many buoyancy-induced flows. Flows adjacent to discrete elements on circuit boards, flows in partially open enclosures, and fire induced flows interacting with vertical surfaces require consideration of the non-boundary-layer effects which arise in the leading edge entrainment region of such surfaces, and in the entrainment regions farther away from such surfaces. The assessment of such induced motion pressure fields is very important in determining the actual flow and the upstream effects associated with such mechanisms.

Many studies have examined the buoyancy-induced flow adjacent to an isothermal vertical surface. Early studies concerned only the approximation of boundary layer formulations. Later and more extensive studies of such transport have led to higher order matched

asymptotic approximate solutions of some of the additional effects in the Navier–Stokes equations. Recently, the effects of the motion pressure, and the resulting entrainment flow and growth of disturbances in transient flows have been studied. A comprehensive summary of such studies may be found in Gebhart *et al.* [1].

1.1. *Early boundary layer studies*

The experiments of Schmidt and Beckmann [2] first demonstrated that the flow of air adjacent to a heated vertical surface formed a boundary layer, as described by Prandtl [3] for forced flows. They also described the similarity solution for this flow found by E. Polhaussen, for a Prandtl number, $Pr = \nu/\alpha$, of 0.733, where α is the thermal diffusivity. Many researchers have extended this analysis to include other values of the Pr and many other surface boundary conditions. Schuh [4] numerically integrated these equations for $Pr = 10, 100, 1000$. Ostrach [5] numerically integrated the similarity equations for a range of Pr including those of liquid metals, $0.01 < Pr < 100$. LeFevre [6] transformed the similarity equations, for asymptotically large and asymptotically small Pr. These equations were then numerically integrated to determine the extreme Pr behavior. Nachtsheim and Swigert [7] derived a method by which the similarity equations may be numerically integrated to within an arbitrary accuracy.

The Navier–Stokes equations, including buoyancy, govern this diffusion field. The flow-generated motion pressure is a part of the complete formulation. In an analysis, streamwise boundary conditions are required along the surface and beyond the upstream and downstream boundaries of the flow domain. However, boundary layer approximations simplify the full equations including buoyancy, by assuming a zero flow and motion pressure ahead of the leading edge of flow. This assumption removes the motion pressure as a dependent variable and leaves only the x- and y-direction velocities, and the temperature, to be calculated for the buoyancy-driven flow. That is, the y-direction force–momentum balance is omitted. The y-direction velocity is then found by using mass continuity considerations. The full equations are further simplified by neglecting the streamwise diffusion of momentum and energy in this flow. That is, parallel to the surface, information may travel in only the downstream direction. These simple boundary layer equations then require streamwise-direction boundary conditions only at the upstream boundary of the computational domain. No boundary conditions are needed for the motion pressure, which has been ignored in the boundary layer formulation. Therefore, the boundary layer approximations commonly apply only at downstream locations. These are conventionally taken to be in terms of the local Grashof number, Gr, greater than 10^4. The effects of motion pressure, and of streamwise diffusion, are very important at smaller values of Gr and in the entrainment regions outside the boundary layer.

The simple boundary layer formulation allows similarity solutions for many kinds of imposed surface conditions. All require a zero fluid velocity at the leading edge. Figure 2(a) shows the calculated streamlines, for $Pr = 0.72$. The entrainment flow, toward the leading edge, amounts to zero shear flow adjacent to a horizontal isothermal surface, at the temperature of the ambient fluid. Past finite difference calculations, using velocity and temperature variables, commonly retain this zero streamwise velocity condition at the leading edge. This measure reduces the mass flow rate calculated in the downstream flow. Also, an unrealistically high y-direction entrainment velocity arises at the leading edge. This effect reduces the error in the calculated downstream mass flow rate.

Figure 2(b) illustrates the effect of the boundary layer approximation on the temperature field. Neglecting streamwise diffusion suppresses the temperature excess over the ambient temperature, t_∞, in the approaching flow region. A temperature effect upstream, due to thermal conduction, is not predicted, using the boundary layer approximation. The physical extent of this field is determined by Pr. The extent of this upstream diffusion increases with decreasing Pr, that is, with increasing α. Omitting the actual streamwise conduction results in an infinite temperature gradient near the leading edge, as indicated by the convergence of the isotherms at $x = 0$, in Fig. 2(b). This lack of realism results in the prediction of an infinite local heat flux there. This is integratable, under some imposed conditions.

1.2. *Higher order approximations*

Some past analyses have improved the accuracy of the transport near the leading edge. The pressure and the tangential diffusion terms may be retained in the Navier–Stokes formulation, for transient flows and for flows at small Gr. Sugawara and Michiyoshi [8] calculate the flow due to a step change in the temperature of a semi-infinite surface having a leading edge. Convection terms were ignored in the calculation of the initial response. After completion of the one-dimensional early transient response, the full Navier–Stokes formulation was used to continue the calculation. Yang and Jerger [9] and Kadambi [10] used perturbation analyzes for moderate Gr. The boundary layer solution was the first term in the series.

Hieber [11] corrected an error due to improper matching considerations in Kadambi [10] and also extended the corrected results, in a second order expansion. A first order correction to the global heat transfer arose. This correction did not arise from local conductive heat transfer from the surface. Instead, it was attributed to the presence of a leading edge. This increased global heat transfer is analogous to the increase in surface shear stress found for forced flow over a flat surface with a leading edge, described by

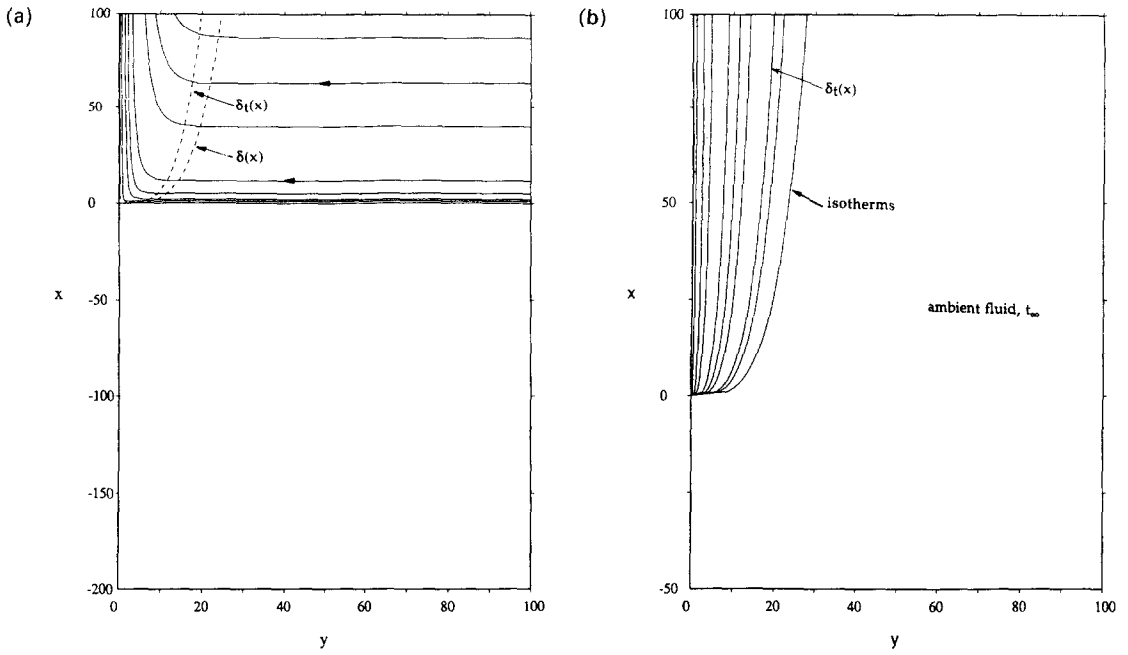

FIG. 2. (a) Streamlines based on boundary layer assumptions, $Pr = 0.72$; (b) isotherms based on boundary layer assumptions, $Pr = 0.72$.

Imai [12]. The perturbation expansion parameter is proportional to negative powers of Gr. This makes the inner solutions of both temperature and velocity singular at the leading edge. The outer temperature field is assumed to be everywhere at the ambient temperature. Conduction ahead of the leading edge is not included, similar to boundary layer theory. Also, the singularity of the perturbation parameter does not allow any calculation of the motion pressure to be calculated at the leading edge. There, it would be expected to have its largest magnitude.

Jaluria [13] used a finite difference calculation to model the natural convection flow near several discrete uniform heat flux sources. These sources were imbedded in an otherwise adiabatic vertical surface. The first of the discrete uniform heat flux sources was located at the leading edge of the vertical surface. The model neglected flow entrainment from upstream of the leading edge of the surface. A streamfunction-vorticity formulation of the full equations was used to model the flow, for small Gr. The boundary layer equations were solved to represent the flow at large Gr. The matching of the boundary layer solution to the solution of the full equations provided the outflow boundary conditions needed for the solution of the full equations.

1.3. *Measurements related to motion pressure effects on entrainment*

Early measurements by Pera and Gebhart [14] determined the interaction between plane thermal plumes and neighboring surfaces. Plumes adjacent to a vertical wall were found to attach to the surface, downstream. The underlying mechanism for this interaction was calculated to be a negative motion pressure field induced by the plume. The restricted entrainment between the plume and an adjacent surface causes a motion pressure deficit in the region between the plume and the surface. The higher ambient pressure on the other side of the plume, in a region of unrestricted entrainment, inclines the plume toward the surface.

Agarwal and Jaluria [15] used a numerical calculation to model the flow of a thermal plane plume in close proximity to a vertical adiabatic surface. The computational domain was divided into two regions, as done by Jaluria [13]. The downstream outflow boundary conditions for the full equations were found by matching, using a boundary layer type solution, at suitably large Gr. Agarwal and Jaluria [15] first discuss calculations which did not include the induced entrainment flow, which arises from below the heat source. Subsequent calculations included some induced entrainment upflow. The motion pressure effect across the plume was computed at several downstream positions, neglecting the upflow entrainment. The plume was deflected, towards the vertical surface, by the flow-induced pressure deficit between the vertical surface and the plume, as found by Pera and Gebhart [14]. Agarwal and Jaluria calculated the difference between the pressure near the surface and in the ambient region. It is greatest near the plume source and diminishes downstream. Agarwal and Jaluria [15] discuss measurements of the position of the plume centerline, made using shadow-graphs. These measurements confirm the numerical predictions. Measurements of the temperature profile of the plume verified the temperature calculations.

Disturbance growth, during the beginning of transient flows, is apparently driven by the motion pressure field. This develops early in the flow. Joshi and Gebhart [16, 17] report detailed measurements of disturbance growth in a flow developing adjacent to a vertical surface, subject to a sudden imposition of a surface energy flux. Temperature disturbances were measured prior to the passage of the leading edge effect. Pressure disturbances are the likely mechanism by which disturbance information travels downstream, just ahead of or during the propagating leading edge effect. This may also be a mechanism for disturbance travel in flows after the leading edge effect has passed. Clearly, the motion pressure field must be included to model fully both the disturbance growth and propagation in such flow regions.

1.4. *Related studies of motion pressure effects on entrainment*

Boundary layer and higher order approximations have been evaluated for the flow in the boundary region, downstream of the leading edge. The determination of the flow around the leading edge, and in the distant entrainment regions, requires an investigation of several more subtle effects. The density difference, and the buoyancy force, are usually small around the surface leading edge and, also, in distant entrainment regions. Motion pressure gradients drive the in-flow. Also, in this region of relatively low velocity, thermal and momentum diffusion upstream may be significant. The full equations, including the motion pressure field and the streamwise diffusion terms, must be used to describe the flow. The x-direction diffusion terms require the specification of x-direction boundary conditions at two locations. One is commonly specified at the upstream leading edge. The other is usually specified at some downstream outflow location. This downstream location is at a value of Gr large enough that the boundary layer approximations apply. Several recent studies have considered the motion pressure field and its effect on the entrainment flow.

Riley [18] analyzed the flow above a horizontal line source in an extensive quiescent fluid. The plume flow, and the entrainment flow, were calculated using inner and outer perturbation expansions, respectively. The entrainment flow was also calculated for the addition of an adiabatic horizontal surface, below the line source. The entrainment flow, in the absence of a horizontal surface, was an upflow throughout the entrainment region. The addition of an adiabatic horizontal surface, below the line source, substantially changed this entrainment flow. The upstream entrainment flow changed from an upflow to a predominantly horizontal in-flow. Above the line source, the entrainment flow develops a downward component. The relative strength of this component increases downstream of the line source. Riley [18] also estimated the effect of an adiabatic vertical surface adjacent to an otherwise unrestricted entrainment flow. A downward component of the entrainment flow was calculated, on the unbounded side of the plume. An approximate calculation of the motion pressure difference across the plume indicated that the gradient deflects the plume towards the vertical surface.

Afird and Zebib [19] considered the natural convection air cooling of single and multiple uniformly heated devices mounted on a vertical surface. The effect of conduction, in the solid elements, was included in this analysis. A two-dimensional rectangular region was modeled, with the surface containing the heated devices at one side. The entrainment flow was assumed to cross normal to the boundaries of the modeled rectangular region. The streamlines and isotherms were, thus, assumed to be normal to the chosen distant boundaries. To produce such a flow may require additional, tacitly assumed, forces on the fluid in this, otherwise, inviscid region. The influence of distant boundary conditions is small, at the surface. The model may, then, accurately predict the flow adjacent to the surface, in the boundary layer region. However, such boundary conditions will not adequately model the entrainment flow, which is driven solely by the induced motion pressure field. Afird and Zebib [19] formulated the model using velocity, temperature and pressure as dependent variables. Results were not given for the induced pressure field, which is a part of the flow solution.

A finite element analysis, by Pelletier *et al.* [20], modeled buoyancy-induced flows in a square cavity, in an annulus and adjacent to a finite vertical plane surface. The results, near the surface, for a flow adjacent to a vertical flat surface with a leading edge, in an extensive medium, were in good agreement with previous results. The entrainment flow streamlines crossed normal to the distant boundaries of the modeled region. As with the results of Afird and Zebib [19], such a flow may require additional and tacitly assumed forces on the fluid in this inviscid region. This indicates that a force, other than the induced motion pressure field, is also acting on this inviscid entrainment flow. Pressure contours were shown, but were not compared with inviscid flow results in the entrainment flow region. The isobars were not shown in the distant entrained flow region.

1.5. *Current study*

There has been very little modeling effort concerning the motion pressure effects which arise in buoyancy-induced flows, even though such induced flow effects often determine the local flow. The largest magnitude of these effects commonly arises near the leading edge of the surface. The boundary layer equations do not apply there. Motion pressure is the dominant force in these entrainment region transport processes. The motion pressure field determines the flow effects in the whole region near the leading edge. These are nonboundary layer flows. Calculation of

additional nonboundary layer mechanisms clearly requires the accurate determination of the pressure gradients over the whole entrainment region. These mechanisms are of increasing importance in the modeling of disturbance growth in developing flows and in the modeling of transport near small and discrete heat sources, which are of increasing importance in many applications.

In the present study, the two-dimensional Navier–Stokes and energy equations, that is, the full equations, have been integrated numerically, for steady-state flow. No boundary layer approximations were used. These equations apply throughout the flow region and, therefore, govern both the inner viscous and the outer inviscid regions. The equations are written by replacing the velocity–pressure transport formulation by the streamfunction–vorticity formulation. By the use of algebraic transformations, the surface and a large part of the distant entrainment region are modeled simultaneously. Accurate estimates of the distant boundary conditions are obtained by placing region boundaries far from the surface, in regions of very small velocity, temperature and pressure gradients. Thereby, the steady-state velocity and temperature fields may be calculated, without the need to determine simultaneously the motion pressure. The Poisson equation, for the pressure field, is then derived from the momentum equations. It is then numerically integrated to determine the associated motion pressure field throughout the region.

2. FORMULATION

2.1. *Equations of conservation of mass, momentum and energy*

The full Navier–Stokes and energy equations, using the Boussinesq approximations, model this flow adjacent to an isothermal vertical surface in an extensive, quiescent medium. Recall Fig. 1. The energy effects of viscous dissipation and pressure work are neglected. See Gebhart *et al.* [1], p. 29. The time-dependent form, in dimensional variables and Cartesian coordinates, is

$$\frac{\partial \bar{u}}{\partial \bar{x}} + \frac{\partial \bar{v}}{\partial \bar{y}} = 0 \tag{2a}$$

$$\frac{\partial \bar{u}}{\partial \bar{\tau}} + \bar{u}\frac{\partial \bar{u}}{\partial \bar{x}} + \bar{v}\frac{\partial \bar{u}}{\partial \bar{y}} = \nu\left(\frac{\partial^2 \bar{u}}{\partial \bar{x}^2} + \frac{\partial^2 \bar{u}}{\partial \bar{y}^2}\right) - \frac{1}{\rho}\frac{\partial \bar{p}}{\partial \bar{x}} + g\beta(\bar{t} - \bar{t}_\infty) \tag{2b}$$

$$\frac{\partial \bar{v}}{\partial \bar{\tau}} + \bar{u}\frac{\partial \bar{v}}{\partial \bar{x}} + \bar{v}\frac{\partial \bar{v}}{\partial \bar{y}} = \nu\left(\frac{\partial^2 \bar{v}}{\partial \bar{x}^2} + \frac{\partial^2 \bar{v}}{\partial \bar{x}^2}\right) - \frac{1}{\rho}\frac{\partial \bar{p}}{\partial \bar{y}} \tag{2c}$$

$$\frac{\partial \bar{t}}{\partial \bar{\tau}} + \bar{u}\frac{\partial \bar{t}}{\partial \bar{x}} + \bar{v}\frac{\partial \bar{t}}{\partial \bar{y}} = \alpha\left(\frac{\partial^2 \bar{t}}{\partial \bar{x}^2} + \frac{\partial^2 \bar{t}}{\partial \bar{y}^2}\right), \tag{2d}$$

where $\bar{x}$ and $\bar{y}$ are the dimensional Cartesian coordinates. Also, $\bar{\tau}$ is the time from some initial datum, $\bar{u}$ and $\bar{v}$ are the velocities in the $\bar{x}$- and $\bar{y}$-directions, respectively, $\bar{t}$ is the local fluid temperature, $\bar{p}$ is the local motion pressure, α is the thermal diffusivity and ν is the kinematic viscosity. The motion pressure is the local static pressure less the remote ambient hydrostatic pressure.

2.2. *Approximation of the boundary conditions*

Boundary conditions for these equations are to be defined on all boundaries. Those at the surface are the familiar conditions for a no-slip surface and local accommodation at the interface region. Both of the velocity components are zero and the temperature of the fluid is the assigned surface temperature, here assumed to be uniformly t_0. Boundary conditions of symmetry, in y, are imposed along $y = 0$, ahead of the leading edge. In the limits $\bar{x} \to -\infty$ and $\bar{y} \to \infty$, these boundary conditions are those of an inviscid flow and a distant ambient temperature. The boundary conditions are written as

$$\bar{y} = 0, \bar{x} \geqslant 0: \quad \bar{u} = \bar{v} = 0, \bar{t} = t_0 \tag{3a}$$

$$\bar{y} = 0, \bar{x} < 0: \quad \partial \bar{u}/\partial \bar{y} = \bar{v} = \partial \bar{t}/\partial \bar{y} = 0 \tag{3b}$$

$$\bar{y} \to \infty: \quad \partial \bar{u}/\partial \bar{y} = \partial \bar{v}/\partial \bar{x}, \bar{t} = t_\infty \tag{3c}$$

$$\bar{x} \to -\infty: \quad \partial \bar{u}/\partial \bar{y} = \partial \bar{v}/\partial \bar{x}, \bar{t} = t_\infty. \tag{3d}$$

The full equations contain second order partial derivatives of the velocities and temperature fields in both the x- and y-directions. Therefore, two boundary conditions, one for each of the x- and the y-directions, are needed for the temperature and both components of velocity. Recall that the boundary layer equations neglect streamwise diffusion and, therefore, contain only first order partial derivatives in the x-direction. These equations then require only one x-direction boundary condition for each of the temperature and the two velocity components. These are specified at the upstream boundary, located at $Gr = 0$.

At the computational outflow boundary, where $Gr_{\max} = 10^6$, the exact boundary conditions are not immediately apparent. Jaluria [13] and Agarwal and Jaluria [15] have modeled the outflow boundary conditions for the full equations by matching the numerically integrated solution of the boundary layer equations with the numerically integrated solution of the full equations. For any given outflow boundary location, Jaluria [13] and Agarwal and Jaluria [15] moved the location of the matching location of the solutions downstream until there remained no appreciable change in their results. The boundary layer equations provide a good approximation of the flow adjacent to the surface, for sufficiently large Gr. However, these equations are not valid further out from the surface, in the region of the inviscid entrained flow. A different approach was taken here. Roach [21] suggests that the least restrictive outflow boundary condition, which allows convergence of the streamfunction in numerical forced flow calculations, is a zero streamwise second derivative of the streamfunction. This outflow boundary condition

requires the specification of the streamfunction, or its first derivative, at the other boundaries. Here, the streamwise second derivative of the streamfunction is specified as zero, that is $\partial^2\psi/\partial x^2 = 0$, at Gr_{max}. Likewise, the streamwise diffusion of temperature is specified to be zero, $\partial^2 t/\partial x^2 = 0$, at Gr_{max}. This temperature boundary condition, neglecting streamwise diffusion, is consistent with the boundary layer theory approximations.

2.3. *Generalized scaled variables*

Nondimensionalization of the equations requires characteristic values for the dependent and independent variables. However, there is no apparent length scale for the configuration considered here. The surface length is not specified a priori. Instead, it will be determined as the length at which $Gr = 10^6$, where boundary layer assumptions may be applied. The surface is immersed in an extensive medium, which extends indefinitely outward from the surface, on both sides, and downstream from the leading edge. Also, there are no readily apparent choices for the characteristic velocity, the characteristic time or the characteristic motion pressure in this buoyancy-induced flow. Instead, the variables are scaled by choosing a characteristic length such that $Gr = 1$, at the characteristic length. The other characteristic quantities are defined in such a way as to be consistent with the above characteristic length. See Wright [22] for the details. Undefined variables are substituted into equations (2). The physical variables are written in terms of the following six corresponding nondimensional variables and the characteristic values as

lengths:

$$\bar{x} = x\left[\frac{\nu^2}{g\beta(\bar{t}_0-\bar{t}_\infty)}\right]^{1/3} \quad \bar{y} = y\left[\frac{\nu^2}{g\beta(\bar{t}_0-\bar{t}_\infty)}\right]^{1/3} \tag{4a, b}$$

velocities:

$$\bar{u} = u[g\beta(\bar{t}_0-\bar{t}_\infty)\nu]^{1/3} \quad \bar{v} = v[g\beta(\bar{t}_0-\bar{t}_\infty)\nu]^{1/3} \tag{4c, d}$$

temperature and pressure:

$$\phi = \frac{\bar{t}-\bar{t}_\infty}{\bar{t}_0-\bar{t}_\infty}, \quad \text{and} \quad \bar{p} = p\rho[g\beta(\bar{t}_0-\bar{t}_\infty)\nu]^{2/3}. \tag{4e, f}$$

Typical values correspond to a temperature excess $t_0-t_\infty = 10°C$ and properties evaluated at 22°C. The characteristic length is then 0.89 mm for air and 0.77 mm for water. The characteristic velocity is 17.2 mm s^{-1} for air and 2.7 mm s^{-1} for water. The magnitude of the characteristic motion pressure, p, is 0.35×10^{-3} Pa for air and 7.1×10^{-3} Pa for water.

Substituting the above expressions for the dimensional variables into equations (2) leads to the following dimensionless forms

$$\frac{\partial u}{\partial x}+\frac{\partial v}{\partial y} = 0 \tag{5a}$$

$$\frac{\partial u}{\partial \tau}+u\frac{\partial u}{\partial x}+v\frac{\partial u}{\partial y} = \left(\frac{\partial^2 u}{\partial x^2}+\frac{\partial^2 u}{\partial y^2}\right)-\frac{\partial p}{\partial x}+\phi \tag{5b}$$

$$\frac{\partial v}{\partial \tau}+u\frac{\partial v}{\partial x}+v\frac{\partial v}{\partial y} = \left(\frac{\partial^2 v}{\partial x^2}+\frac{\partial^2 v}{\partial y^2}\right)-\frac{\partial p}{\partial y} \tag{5c}$$

$$\frac{\partial \phi}{\partial \tau}+u\frac{\partial \phi}{\partial x}+v\frac{\partial \phi}{\partial y} = \frac{1}{Pr}\left(\frac{\partial^2 \phi}{\partial x^2}+\frac{\partial^2 \phi}{\partial y^2}\right). \tag{5d}$$

2.4. *Streamfunction–vorticity formulation of the conservation equations*

These equations are in terms of the velocity, temperature and motion pressure fields. The solution for the motion pressure, in an external incompressible flow, is very sensitive to the boundary conditions and generally converges slowly. See Roache [21]. A method often used to eliminate the need to calculate the motion pressure, concurrently with the flow field, is to introduce a streamfunction which satisfies the continuity equation. This allows the two momentum equations to be replaced by a vorticity transport equation, along with a Poisson equation for the streamfunction. A Poisson equation, for motion pressure, is derived from the momentum equations. The flow field is then calculated independently from the motion pressure field. After the flow field has been determined, the motion pressure field may be calculated in a straight-forward manner.

The streamfunction, ψ, implicitly defined as $u = \partial\psi/\partial y$ and $v = -\partial\psi/\partial x$, satisfies equation (5a), automatically. Differentiating equation (5b) by y and equation (5c) by x and subtracting the results yields the vorticity transport equation

$$\frac{\partial \omega}{\partial \tau}+\frac{\partial \psi}{\partial y}\frac{\partial \omega}{\partial x}-\frac{\partial \psi}{\partial x}\frac{\partial \omega}{\partial y} = \left(\frac{\partial^2 \omega}{\partial x^2}+\frac{\partial^2 \omega}{\partial y^2}\right)-\frac{\partial \phi}{\partial y}, \tag{6}$$

where the vorticity, ω, is defined as

$$\omega = -\left(\frac{\partial^2 \psi}{\partial x^2}+\frac{\partial^2 \psi}{\partial y^2}\right) = -\nabla^2\psi. \tag{7}$$

Equation (5d) for temperature excess, ϕ, becomes

$$\frac{\partial \phi}{\partial \tau}+\frac{\partial \psi}{\partial y}\frac{\partial \phi}{\partial x}-\frac{\partial \psi}{\partial x}\frac{\partial \phi}{\partial y} = \frac{1}{Pr}\left(\frac{\partial^2 \phi}{\partial x^2}+\frac{\partial^2 \phi}{\partial y^2}\right). \tag{8}$$

Equations (6)–(8), with the appropriate boundary conditions, determine the flow field.

Boundary conditions for these equations are derived from the boundary conditions which apply to the equations in velocity and temperature variables. Along the $y = 0$ axis these are written as

$$y = 0, 0 \leqslant x \leqslant 100: \quad \psi = 1-\phi = 0, \omega = -\partial^2\psi/\partial^2 y \tag{9a}$$

$$y = 0, x < 0: \quad \psi = \omega = \partial\phi/\partial y = 0. \tag{9b}$$

The ambient fluid is truly quiescent only at an infinite distance away from the surface, in the steady-state flow. As seen in Fig. 3(a), the distant boundaries in this calculation are set at large, but finite, distances from the surface. Distant boundary conditions must be determined which appropriately approximate the

infinite boundary conditions. Far from the surface, the temperature excess and the vorticity must be zero, unchanged from that of a quiescent fluid. Preliminary calculations were used to determine the distance at which these distant boundary conditions of zero temperature excess and zero vorticity may be imposed. Increasing the distance of the boundaries, from the surface, changed the calculated values of the streamfunction and vorticity by less than 10^{-6}. The requirements, consistent with these conditions, were

$$x = -1000: \quad \omega = \phi = 0$$

and

$$y = 1000: \quad \omega = \phi = 0. \tag{10}$$

The boundary conditions on the streamfunction, based on the condition of zero vorticity at distant boundaries and on the definition of the streamfunction in equation (7), are

$$x = -1000: \quad \nabla^2\psi = 0$$

and

$$y = 1000: \quad \nabla^2\psi = 0. \tag{11}$$

These conditions are consistent with having specified zero vorticity at the distant boundaries.

Consistent with this full formulation, the streamwise diffusion terms are retained everywhere, except at the upper streamwise outflow boundary. There, the boundary conditions were chosen as

$$y > 0, \quad x = x_{\max}:$$
$$\partial^2\psi/\partial x^2 = \partial^2\omega/\partial x^2 = \partial^2\phi/\partial x^2 = 0. \tag{12}$$

Specifying the second streamwise derivatives of the vorticity and the temperature excess as zero is consistent with the boundary layer theory condition of no downstream diffusion of momentum or of thermal energy. The zero second derivative of the streamfunction specifies that the horizontal velocity component is uniform across the outflow boundary, at $Gr_{\max} = 10^6$. As mentioned above, Roache [21] suggests that this outflow boundary condition is the best model of the physical circumstance which still allows for convergence of the equation for the streamfunction. The error introduced by this assumption was minimized in the numerical formulation by specifying a very fine grid spacing in the streamwise direction, at the outflow boundary.

2.5. *Motion pressure equation formulation*

After the flow field has been calculated, the motion pressure field may be determined. The Poisson equation for motion pressure is derived from equations (5b) and (5c). After steady flow is established in the calculations, the transient terms in the momentum equations have become zero. The steady forms of equations (5b) and (5c) are then differentiated with respect to x and y, respectively. Adding the differentiated equations (5b) and (5c) yields the Poisson equation for pressure. The viscous terms of this Poisson equation satisfy equation (5a), identically. The equation for pressure then simplifies to

$$\frac{\partial^2 p}{\partial x^2}+\frac{\partial^2 p}{\partial y^2} = \frac{\partial \phi}{\partial x}-\left[\left(\frac{\partial u}{\partial x}\right)^2+2\frac{\partial u}{\partial y}\frac{\partial v}{\partial x}+\left(\frac{\partial v}{\partial y}\right)^2\right]. \tag{13}$$

The terms on the right-hand-side of equation (13) contain squared first order derivatives. These terms may be simplified by first squaring the mass continuity equation, equation (5a), and writing the result as

$$\left(\frac{\partial u}{\partial x}\right)^2+\left(\frac{\partial v}{\partial y}\right)^2 = -2\frac{\partial u}{\partial x}\frac{\partial v}{\partial y}. \tag{14}$$

When this result is substituted into equation (13), the equation for motion pressure becomes

$$\frac{\partial^2 p}{\partial x^2}+\frac{\partial^2 p}{\partial y^2} = \frac{\partial \phi}{\partial x}+2\left(\frac{\partial u}{\partial x}\frac{\partial v}{\partial y}-\frac{\partial v}{\partial x}\frac{\partial u}{\partial y}\right). \tag{15}$$

All the terms on the right-hand-side of equation (15) are known, after the calculation of the flow field. The Bernoulli equation may then be used, in the inviscid region, to determine the motion pressure far from the surface. At the upper outflow boundary, the streamwise pressure gradient is specified as zero, consistent with conventional boundary layer theory. Along the $y = 0$ axis, ahead of the leading edge, symmetry boundary conditions are used. Adjacent to the surface, the pressure gradient may be calculated from equation (5c). The resulting boundary conditions for the pressure field are then

$$y = 0, 100 \geqslant x \geqslant 0: \quad \partial p/\partial y = \partial^2 v/\partial y^2 \tag{16a}$$
$$y = 0, x < 0: \quad \partial p/\partial y = 0 \tag{16b}$$
$$y = 1000: \quad p = v^2/2 \tag{16c}$$
$$x = -1000: \quad p = u^2/2 \tag{16d}$$
$$x = 100: \quad \partial p/\partial x = 0. \tag{16e}$$

3. NUMERICAL INTEGRATION

Equations (6)–(8) are expressed in a finite difference formulation, for numerical integration. The time-dependent nature of the vorticity and temperature transport equations is retained. The integration continues until the changes of temperature and vorticity between successive iterations is less than 10^{-6}, at each node. Time derivatives are written in a first order accurate explicit forward difference form. Second derivatives are calculated by second order accurate central differencing, except at the boundaries. There, a first order accurate one-sided differencing procedure is used, for these second derivative diffusion terms. The convection terms are differenced using the second upwind differencing scheme described by Roache [21]. Roache [21] notes that this formulation of the convection terms yields between first and second order accuracy.

The Poisson equation for the streamfunction is inte-

grated using successive line over-relaxation (SLOR). The derivative in the direction normal to the surface is integrated implicitly. The integration is explicit in the streamwise direction. The velocities are then calculated from the streamfunction, using a first order center-differenced formulation. After the velocity and temperature fields are determined, the motion pressure equation is integrated, using SLOR.

The extent of the field considered in these calculations was determined by preliminary calculations. A surface length, from $x = 0$ to 100, was chosen since this corresponds to a maximum value of $Gr = 10^6$, where the boundary layers are good approximations. The length corresponding to $x = 100$ is 8.9 cm, for air with properties evaluated at 22°C, at a surface temperature excess of $t_0 - t_\infty = 10$°C. For water and the same temperature conditions, the length corresponds to 7.7 cm. The locations of the distant boundaries, at $x = -1000$ and at $y = 1000$, were chosen after preliminary calculations indicated that the calculated flow was not appreciably changed by increasing these distances. For example, changing the distant boundary to $y = 1500$ produced a change in the value of the streamfunction at $y = 1000$ of less than one part in ten thousand.

3.1. *Coordinate transformations*

In the foregoing formulation, the physical coordinates vary as $-1000 \leqslant x \leqslant 100$ and $0 \leqslant y \leqslant 1000$. Figure 3(a) shows the display of computational grid points, in physical space. The coordinate ranges are $-1000 \leqslant x \leqslant 100$ and $0 \leqslant y \leqslant 1000$. The isothermal vertical surface extends from $x = 0$ to 100, along the $y = 0$ axis. The grid lines are seen to be concentrated near the surface, at small y, near the leading edge, at small x, near the outflow boundary, at $x = 100$, and near the distant boundaries, $x = -1000$ and $y = 1000$, to improve the accuracy of the calculations. The very large range of the physical coordinates used, and the variable spacing of the nodes, would require specification of the distance of each node from its neighbors. This would be inconvenient for efficient numerical calculation. Algebraic transformations, one for x and one for y are used to map this physical space (x, y) into the computational space (x', y') in Fig. 3(b). The resulting grid lines in the computational space are chosen to be evenly distributed, for efficient calculation. The additional advantage of these coordinate transformations is that the computational coordinates vary only as $0 \leqslant x' \leqslant 1$ and $0 \leqslant y' \leqslant 1$, over the whole range.

Sills [23] proposed using either a simple trigonometric or a simple algebraic function to transform the computation grid. Each of these transformations mapped the region $0 \leqslant x \leqslant \infty$ into the region $0 \leqslant x' \leqslant 1$. Each transformation has an analytical inverse. A uniform grid in either of the transformed coordinates would group nodes near the origin upon inverse transformation to physical coordinates. Each transformation increases the spacing between the nodes, in the physical x coordinate, as $x \to \infty$, that is, as $x' \to 1$. Riley [24] used an algebraic function to transform coordinates, for a finite difference model of the transient flow adjacent to a sphere. The radial coordinate was transformed such that $1 \leqslant \bar{r} \leqslant \infty$ mapped to $0 \leqslant r \leqslant 1$. The tangential coordinate, θ, was mapped so that $-\pi \leqslant \theta \leqslant \pi$ mapped to $-1 \leqslant \mu \leqslant 1$. The distant boundary conditions were then applied at a very large distance, in physical coordinates, from the sphere.

Other coordinate transformations were also considered. Thompson *et al.* [25] describe other transformations, such as adaptive grids. These grids change the spacing of the initially chosen computational grid, in response to the evolving flow calculation. The grid spacing is reduced in regions of large gradients of a dependent variable, such as velocity. The spacing is increased where the gradients are small. This method is useful for the finite difference modeling of complex geometries, for which regions of large gradients may not be known a priori. Such grids may also be very effective for transient flows in which the region of largest gradients of the dependent variables may change during the calculation.

The physical coordinates of Fig. 3(a) were next transformed to the computational coordinates in Fig. 3(b), in order to approximate better the boundary conditions. The x-coordinate has been transformed by

$$x' = k_1 \exp[-b(x_{\max} - x)] + k_2 \exp[-c(x - x_{\min})] + k_3\left(\frac{x - x_{\min}}{x_{\max} - x_{\min}}\right). \quad (17)$$

The constants, k_1, k_2, k_3, b, c, were chosen based on preliminary calculations, using coarse grid spacings and fewer nodes. The first term, in k_1, maintains a close spacing of the nodes near the streamwise outflow boundary, for accurate modeling. It also closely spaces the nodes in the streamwise direction, near the surface. The second term, in k_2, groups several nodes near the streamwise inflow boundary, that is, near $x = -1000$. This gives a better approximation of the inflow boundary conditions than if a large grid spacing was used. The third term, in k_3, spaces the streamwise nodes through the entrainment region upstream. The node locations are not changed during a calculation. The minimum value of x is set at $x_{\min} = -1000$, 10 times the length of a downstream surface associated with $Gr = 10^6$. This position was specified after preliminary calculations had shown that no change occurred upon moving $x_{\min}$ further downstream from the leading edge.

The y-coordinate transformation is

$$y' = k_4(1 - \exp(-ay)) + (0.9 - k_4)\left(\frac{y}{y_{\max}}\right) + 0.1 \exp(0.1(y - y_{\max})). \quad (18)$$

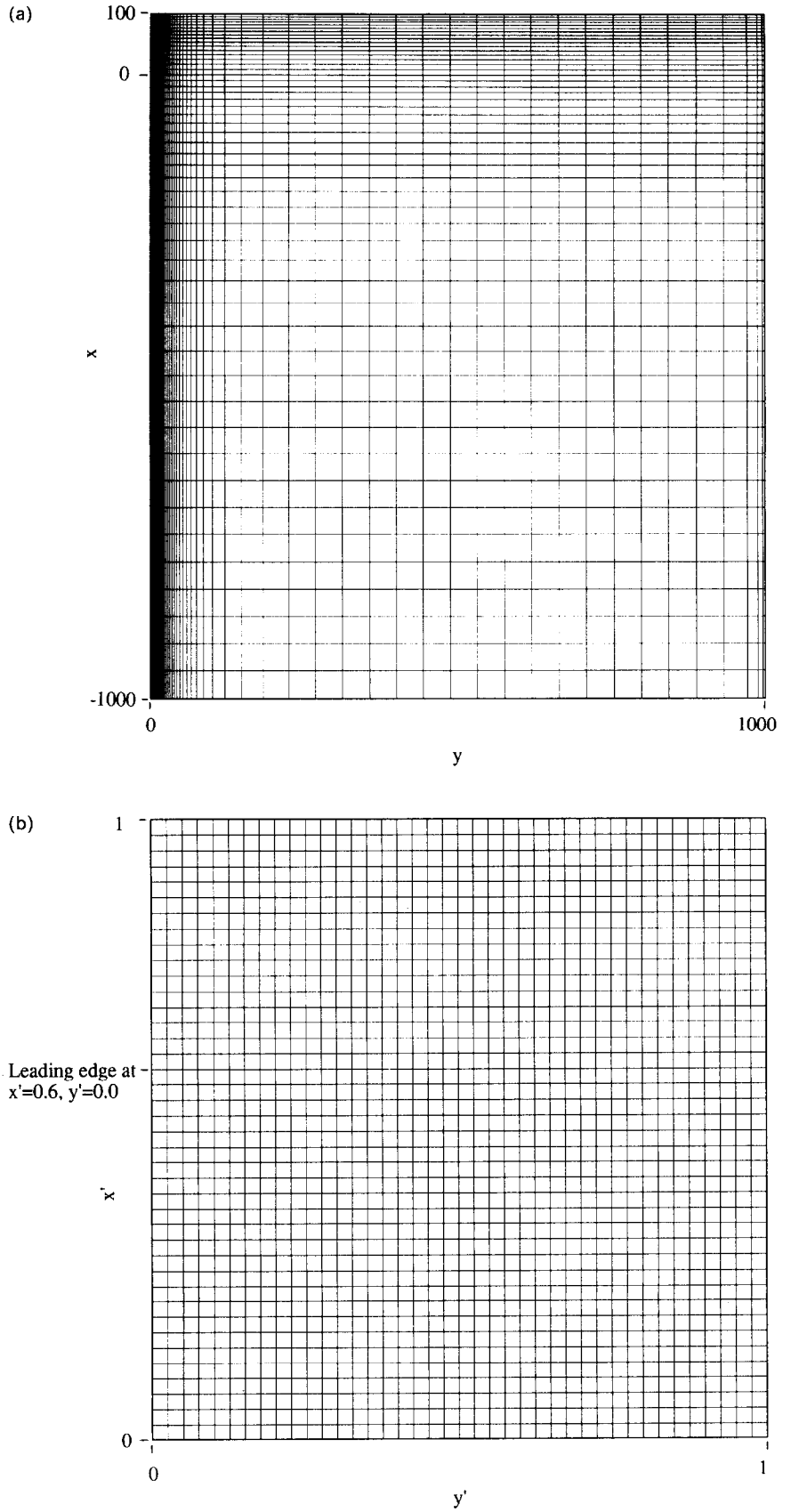

FIG. 3. (a) Numerical grid in physical coordinates, 41×41 nodes. Surface lies from $0 \leqslant x \leqslant 100$ at $y = 0$; (b) numerical grid in computational coordinates, 41×41 nodes.

The constants, k_4 and a, are also based on preliminary calculations. The first term groups 10–20% of the nodes within the nominal boundary layer region. The boundary region is thicker further downstream and contains a higher percentage of the computational nodes than closer to the leading edge. The numerically calculated streamlines in Fig. 4(a) are seen to turn nearly vertical, within this boundary region. A very large density of nodes was required in order to resolve this flow accurately. The third term in equation (18) groups about 5% of the nodes near the distant y-boundary, $y = 1000$. These nodes are required to model accurately the zero shear stress boundary condition, as discussed above. The rest of the nodes are spaced approximately evenly throughout the entrainment region, by the second term in equation (18).

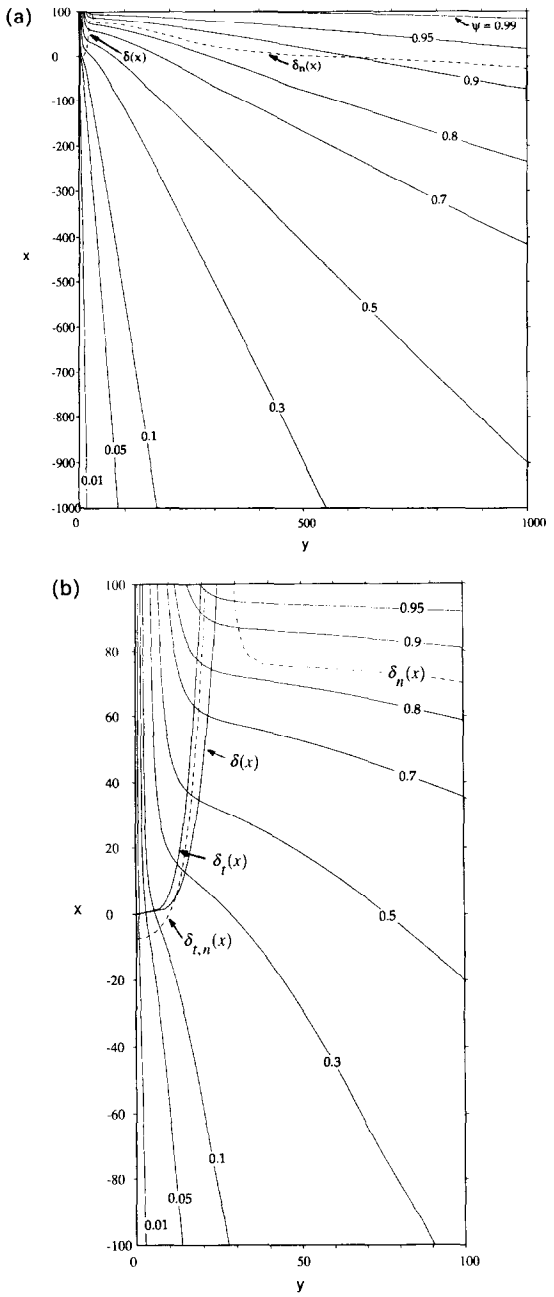

FIG. 4. (a) Streamlines calculated for $Pr = 0.72$ and a maximum $Gr = 10^6$. The velocity boundary layer thicknesses from boundary layer theory and from the finite difference calculation are shown. Surface lies $0 \leqslant x \leqslant 100$; (b) streamlines near the leading edge of the surface calculated for $Pr = 0.72$. Shown for comparison are the temperature and velocity boundary layer thicknesses calculated using boundary layer theory and by the finite difference calculation. Surface lies $0 \leqslant x \leqslant 100$.

3.2. *Transformation parameters*

Transformation parameters and boundary distances for the numerical analysis were determined by the results of preliminary calculations. The location of the boundaries, number of grid points and grid spacing at the boundaries were varied until the calculated results were found to be independent of the grid. The grid spacing near the boundaries was chosen to minimize the error incurred in applying the local boundary conditions. Recall Fig. 3(a). At the boundaries, the calculation of the boundary conditions is often subject to additional errors. This results from the difficulty in modeling the second derivatives and the convection terms at the boundaries. The convection terms for the inflow and the outflow boundary conditions were found to be very sensitive to the node spacing. The nodes at the inflow and outflow boundaries were spaced closely together, to minimize this error. This allowed the first order accurate and one-sided convection approximations, at the boundaries. These approximate the second order accuracy of the second upwind convection term formulation, as used in these calculations. The spacing of the nodes at the outflow boundary, and at the distant x- and y-boundaries, were varied until the solutions remained independent of the grid spacing.

The grid spacing was determined from preliminary calculations. These were to minimize grid-dependent effects. Figure 5 shows the variation of the number of y-direction nodes on the integrated average wall shear

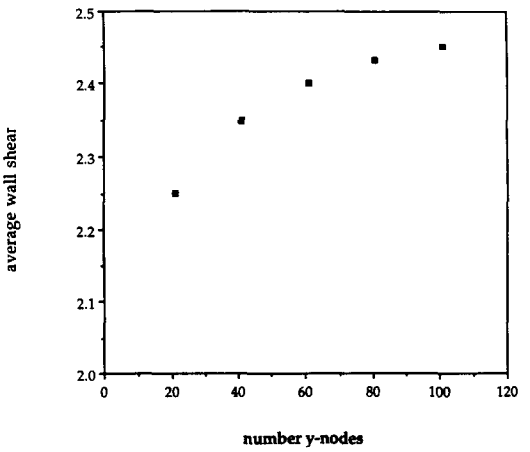

FIG. 5. Variation of calculated wall shear with number of y-direction nodes.

stress. The average wall shear was selected, as a measure of the grid independence, since it is strongly dependent on the y-direction node spacing, adjacent to the vertical surface. Each calculation covered 101 x-direction nodes. The average wall shear reaches an asymptote at about 101 y-direction nodes. The calculated average wall shear varied less with varying number of x-direction nodes. The 101 x-direction nodes were found to provide a grid independent solution.

The transport equations for vorticity and energy, and the Poisson equation for the streamfunction, were numerically integrated until the temperature, vorticity and streamfunction changed less than 10^{-6}, at each grid point, during successive time steps. The flow within the boundary region, adjacent to the surface, converged quickly. For $Pr = 0.72$, the boundary region flow converged after about $\tau = 20$. The distant entrainment flow calculation required $\tau > 180$, for convergence. The temperature excess and vorticity changed slowly, in the leading edge entrainment region. These fields must diffuse away from the surface and into the local entrainment region. This penetration is opposed by the increasing rate of entrainment flow.

After the calculation was terminated, energy and mass balances were calculated for the entire flow field. The calculated thermal conduction rate from the surface was compared with the increased temperature of the fluid flow, throughout the whole computational domain. Also, the mass flow rate across the inflow boundaries was found to be balanced by the flow crossing the outflow boundary. For the energy balance, the difference was less than one part in 10^5. For the mass balance, the difference was less than one part in 10^6.

4. RESULTS

Calculated steady flow results are given for $Pr = 0.72$, typical of air, and $Pr = 6.7$, typical of water. The results are discussed below, in terms of the physical (x, y) coordinates. Comparisons of the finite difference results with similarity solutions of boundary layer flow are shown in the boundary layer similarity coordinate, η. The heated surface is located along the x-axis from $x = 0$ to 100. This range corresponds to a maximum local Grashof number of $Gr_{max} = 10^6$, for both $Pr = 0.72$ and $Pr = 6.7$.

Results are first shown in terms of streamlines and isotherms, for both $Pr = 0.72$ and $Pr = 6.7$. The effect of varying the boundary conditions on the flow is examined. The size of the computational domain is first varied. Then, the distant entrainment flow is compared with an inviscid flow calculation. Next, the new results of the velocity and temperature profiles are compared with those of classical boundary layer theory. These are in good agreement, sufficiently downstream from the leading edge. Then, some of the new results, such as local heat flux and local surface shear stress, are compared with the boundary layer results. Lastly, the resulting calculated motion pressure field is discussed.

4.1. *Calculated flow for* Pr = 0.72

Figure 4(a) shows the streamlines calculated for $Pr = 0.72$. The entire calculated entrainment region is shown. The local velocity boundary layer thicknesses were determined numerically, as $\delta_n(x)$, and by boundary layer theory, as $\delta(x)$, as shown. These thicknesses $\delta_n(x)$ and $\delta(x)$ are defined, for this buoyancy-induced flow, as the distance from the surface at which the streamwise velocity is 1% of the local maximum streamwise velocity, at that value of x. The streamlines in the leading edge entrainment region indicate that the surface is approximately a sink. Over the range of $0 < x \leqslant 100$, the flow is locally more like a boundary layer entrainment flow. Recall Fig. 2(a).

In Fig. 4(a), $\delta_n(x)$ increases as x approaches zero. This contradicts the boundary layer theory result. That theory specifies that the boundary layer thickness approaches zero as x approaches zero. Recall the definition of the $\delta(x)$, as given above. Boundary layer theory also specifies that there is no induced flow ahead of the leading edge. That is, streamwise velocity is taken as zero throughout the entrainment region, $x \leqslant 0$. The new calculations assess the actual flow effects of the induced upstream flow at $x \leqslant 0$. The result is a much larger value for the streamwise velocity, throughout the entrainment region, at $x \leqslant 0$. Thus, a larger boundary layer thickness arises, for this complete numerical calculation, as x approaches zero.

An enlarged region around the leading edge is shown in Fig. 4(b). The actual streamline field shown is to be compared with $\delta(x)$, from boundary layer theory, and $\delta_n(x)$, from the results from these calculations, respectively. In the region downstream of the leading edge, and within $\delta(x)$, the new results are similar to those of boundary layer theory. Recall Fig. 2(a). The streamlines show the flow turning into the vertical buoyancy-driven flow within the boundary layer region.

The entrainment streamlines derived from simple boundary layer theory are identically normal to the surface, everywhere outside the boundary region. Recall Fig. 2(a). That solution is only the first term of the inner expansion of the solution of the full equations. It does not contain any information concerning the distant entrainment flow. The inflow entrainment region shown in Fig. 4(b) also includes the effects of the induced upstream entrainment. The entrainment region streamlines are here calculated to have some upflow component. This effect is similar to the entrainment flow calculated by Hieber [11]. However, those results are not directly comparable, since they apply for a semi-infinite vertical surface beginning at $x = 0$.

The calculated boundary layer thickness, $\delta_n(x)$, shown in Figs. 4(a) and (b), is greater than the bound-

ary layer result, $\delta(x)$. The boundary layer calculations assume no entrainment flow from upstream of the leading edge. Recall Fig. 2(a). Therefore, the boundary layer theory entrainment flow has an unrealistically small u-component and larger v-component, for small values of x, about $x = 0$.

In the entrainment region at $x \leqslant 0$, upstream of the leading edge, the maximum vertical velocity arises along the $y = 0$ streamline. Since this is a line of symmetry, $\partial u/\partial y = 0$. The vanishing first derivative means there must be a local extremum in the streamwise velocity. It is a maximum. Above the leading edge, the entraining flow is retarded by the frictional drag at the surface. The several separated streamlines shown, which indicate the mass flow rate, slant away from the surface. This local effect is quickly overwhelmed, downstream of the leading edge, by fluid entrainment into the rapidly accelerating buoyant flow adjacent to the surface. Downstream of the leading edge, the boundary layer adjacent to the surface forms. The local maximum velocity then moves outward from the $y = 0$ streamline, owing to surface drag. The velocity along the surface remains zero, owing to the no-slip condition. A local maximum streamwise velocity then arises within the downstream developing boundary layer.

4.2. *Variation of the boundary conditions for* Pr = 0.72

Figures 6(a)–(c) show the effects of the chosen distant boundary conditions, at $y = 1000$. These calculations were made using a 61×61 node grid, instead of the 101×101 grid used for the rest of the calculations. The larger grid spacing allowed efficient comparison of many boundary conditions, by reducing the calculation time required for convergence to the steady solution. The 61×61 grid also reduced the resolution of the calculations. This is not an important effect for in comparing boundary conditions. Figures 6(a)–(c) are drawn for y extending to 1500. This allows comparison of the effect of changing the location of the distant y-boundary, on the calculations.

The boundary conditions used to calculate the flow shown in Fig. 6(a) are the same as those used to calculate the flow in Fig. 4(a). The distant y-boundary conditions are specified at $y = 1000$. However, the plotted region is extended to $y = 1500$. The extended plotted region in Fig. 6(a) compares the streamlines with those in Figs. 6(b) and (c). Figure 6(b) shows streamlines calculated for distant y-boundary conditions specified at $y = 1500$. There is no appreciable difference in the position of these sets of streamlines. The $\psi = 0.8$ streamline crosses $y = 1000$ at $x = -190$ for both circumstances, for example. This indicates that $y = 1000$ is suitable for the distant boundary. Figure 6(c) shows streamlines determined by integrating Laplace's equation, $\nabla^2\psi = 0$, for the distant induced inviscid flow region. The distant boundary conditions are the same as those used for the solution of the full equations. The boundary conditions along

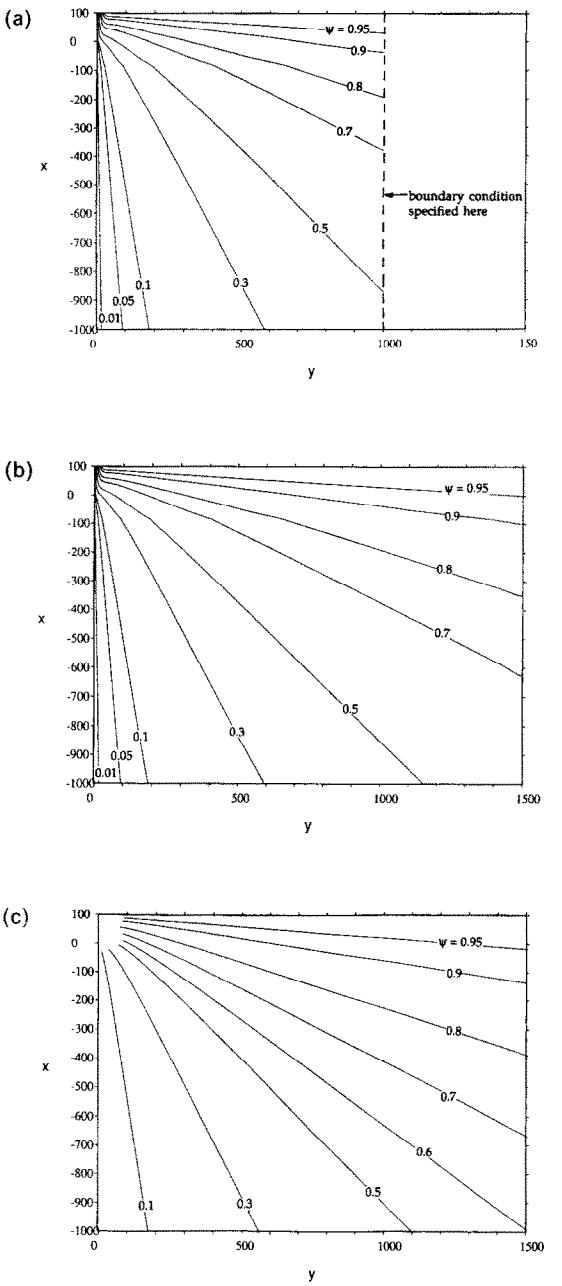

FIG. 6. (a) Streamlines for $Pr = 0.72$ and $Gr_{max} = 10^6$, distant y-boundary set at $y = 1000$. Computational grid is 61×61. Surface lies $0 \leqslant x \leqslant 100$; (b) streamlines for $Pr = 0.72$ and a maximum $Gr = 10^6$, distant y-boundary set at $y = 1500$. Computationl grid is 61×61. Surface lies $0 \leqslant x \leqslant 100$; (c) streamlines from solution of Euler's equations in the entrainment region, for $Pr = 0.72$. The boundary condition for the streamfunction along the vertical surface is $\psi = r^{3/4}$. Surface lies $0 \leqslant x \leqslant 100$.

$y = 0$ are $\psi = 0$, for $x < 0$, and $\psi = r^{3/4}$, $x > 0$, where $r^2 = x^2 + y^2$. This variation of ψ, along $y = 0$, $x = 0$, is the boundary condition for the inviscid outer flow, determined using boundary layer theory. Comparing the streamlines in Fig. 6(c) with those in Figs. 6(a) and (b) indicates that the distant boundary conditions used here, for the entrainment solution of the

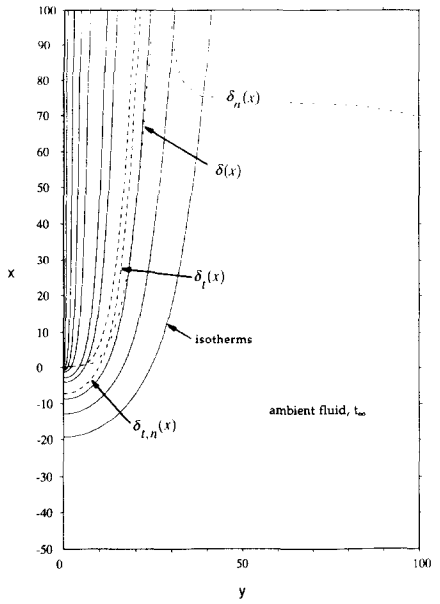

FIG. 7. Isotherms calculated for $Pr = 0.72$. Velocity and temperature boundary layer thicknesses, from finite difference calculation and boundary layer analysis, are shown. Surface lies $0 \leqslant x \leqslant 100$.

streamfunction, are appropriate for the distant flow. The streamlines calculated using the $\psi = r^{3/4}$ boundary condition, at $y = 0$, are for a smaller upflow at the distant boundary. This is shown by the smaller value of $u = \partial\psi/\partial y$, in Fig. 6(c), compared with those in Figs. 6(a) and (b).

The calculated isotherms, $\phi = \text{constant}$, for $Pr = 0.72$, are shown in Fig. 7. The fluid temperature decreases to the ambient temperature, away from the surface. Only the region near the vertical surface has an appreciable temperature excess. The temperature boundary layer thicknesses, $\delta_t(x)$ and $\delta_{tn}(x)$, are shown for reference. The calculated thermal boundary layer thickness, $\delta_{tn}(x)$, agrees well with the result of boundary layer theory, $\delta_t(x)$, for $x > 0$. The effects of upstream conduction, at $x \leqslant 0$, that is, the temperature excess field upstream of the leading edge of the surface are appreciable. The $\phi = 0.01$ isotherm indicates the thermal boundary layer thickness. It extends below the leading edge, to about $x = -7$. This is the temperature effect in the leading edge entrainment region at $x = 0$. The comparable effect on velocity is less, in this leading edge region. This limited penetration of elevated temperature indicates that the motion pressure field induces the entrainment flow in the upstream region.

4.3. *Results for* Pr = 6.7

The results in Fig. 8(a), for $Pr = 6.7$, are similar to those in Fig. 4(a) for $Pr = 0.72$. The principal differences are in the region adjacent to the surface. The enlargement in Fig. 8(b) clarifies the streamlines in the boundary layer region. The actual calculated boundary layer region, $\delta_n(x)$, and the boundary layer theory result, $\delta(x)$, are thicker than for $Pr = 0.72$. Both calculated thermal boundary layer thicknesses, $\delta_t(x)$ and $\delta_{tn}(x)$, are thinner than for the $Pr = 0.72$ results. Isotherms for $Pr = 6.7$ are shown in Fig. 9. The temperature excess is confined to a smaller region than in Fig. 7 for $Pr = 0.72$. This is the expected result for a larger Prandtl number. This suggests an increase in

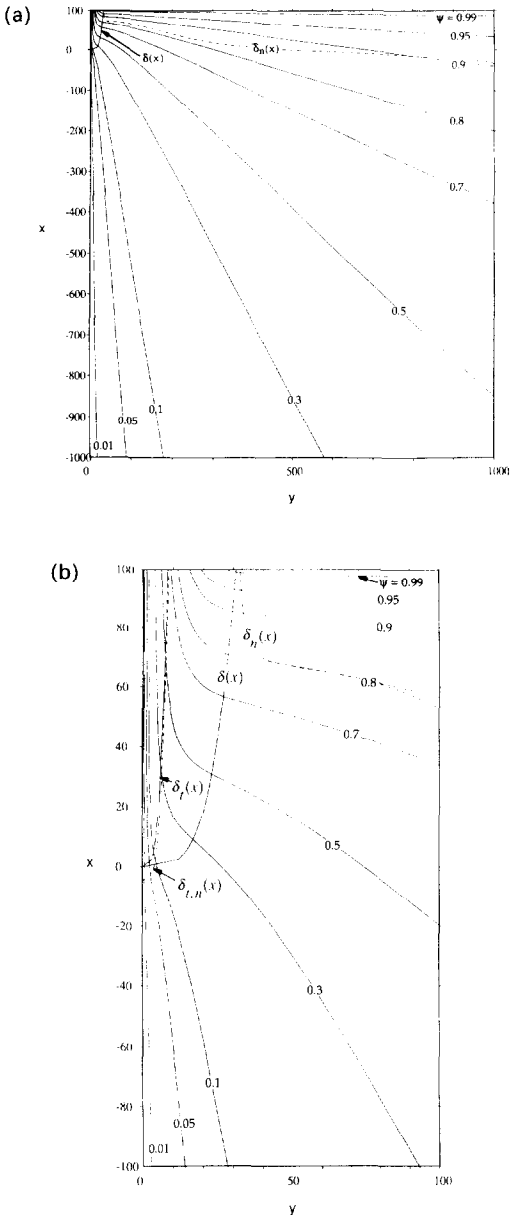

FIG. 8. (a) Streamlines calculated for $Pr = 6.7$ and a maximum $Gr = 10^6$. The velocity boundary layer thicknesses from boundary layer theory and from the finite difference calculation are shown. Surface lies $0 \leqslant x \leqslant 100$; (b) streamlines near the leading edge of the surface calculated for $Pr = 6.7$. Shown for comparison are the temperature and velocity boundary layer thicknesses calculated using boundary layer theory and by the finite difference calculation. Surface lies $0 \leqslant x \leqslant 100$.

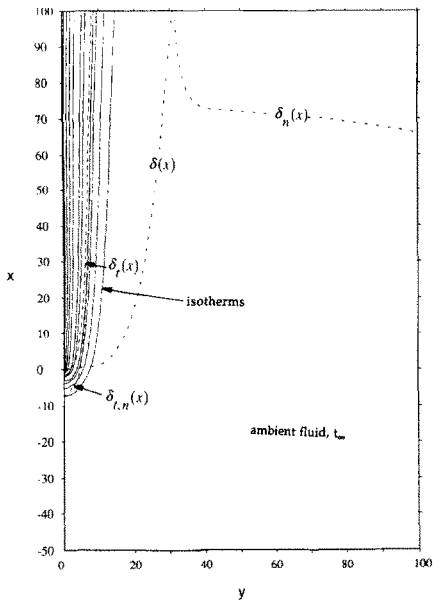

FIG. 9. Isotherms calculated for $Pr = 6.7$. Velocity and temperature boundary layer thicknesses, from finite difference calculation and boundary layer analysis, are shown. Surface lies $0 \leqslant x \leqslant 100$.

viscous effects, relative to the buoyancy force effect in the boundary layer.

4.4. *Further comparison of numerical results and conventional boundary layer theory*

The calculations for $Pr = 0.72$ are further compared below with classical boundary layer theory results. These results follow from similarity analysis. See the many solutions in Gebhart *et al.* [1]. Similar considerations for $Pr = 6.7$ were discussed by Wright [22].

Similarity formulations transform the boundary layer equations from partial to ordinary differential equations. The y-coordinate becomes η. The variables (x, y) are related to the similarity variable, η, as

$$\eta = \frac{y}{x}\left(\frac{Gr_x}{4}\right)^{1/4} = \frac{y}{\sqrt{2}x^{1/4}}. \tag{19}$$

The streamfunction, ψ, is written in terms of a function $f(\eta)$ as

$$\psi(x, y) = 4\nu\left(\frac{Gr_x}{4}\right)^{1/4} f = 2\sqrt{2}\nu x^{3/4} f. \tag{20}$$

The resulting streamwise and entrainment velocities, u and v, are

$$u = \frac{2\nu}{x}(Gr_x)^{1/2}\frac{\mathrm{d}f(\eta)}{\mathrm{d}\eta} = 2\nu x^{1/2} f' \tag{21}$$

$$v = \frac{\nu}{x}\left(\frac{Gr_x}{4}\right)^{1/4}\left(\eta\frac{\partial f}{\partial \eta} - 3f\right)$$

$$= \frac{\nu}{\sqrt{2}x^{1/4}}\left(\frac{y}{\sqrt{2}x^{1/4}} f' - 3f\right), \tag{22}$$

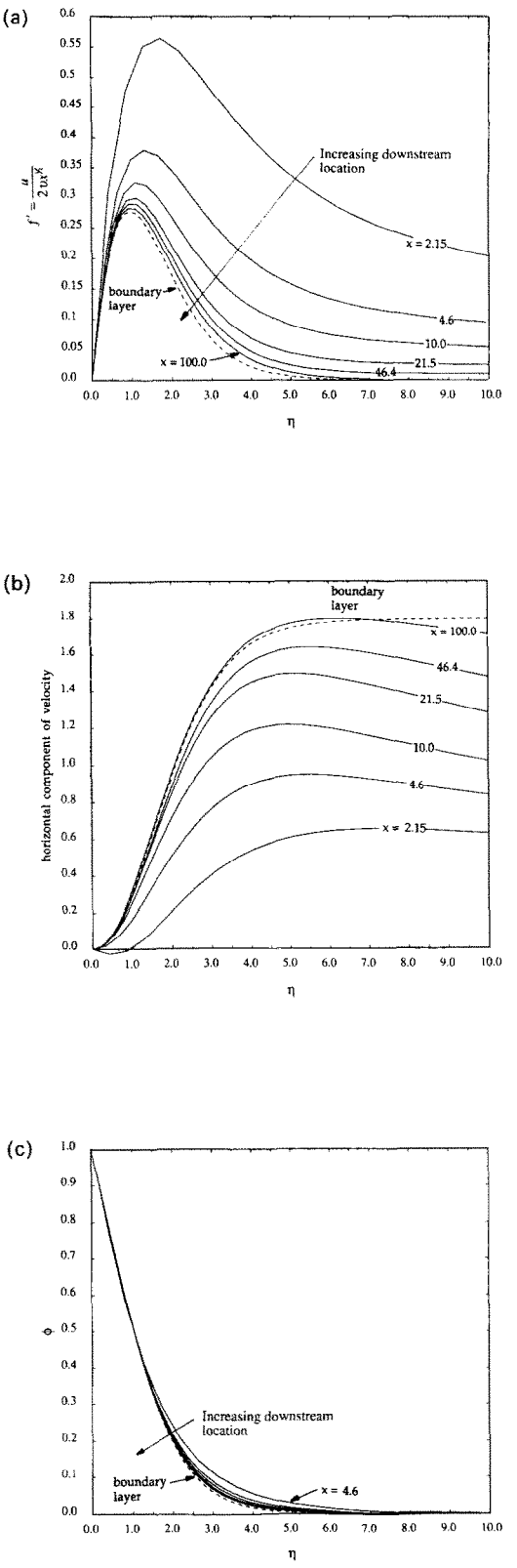

FIG. 10. (a) Calculated streamwise velocity profile compared with the boundary layer theory result, for $Pr = 0.72$; (b) calculated horizontal entrainment velocity profile compared with the boundary layer theory result, for $Pr = 0.72$; (c) calculated temperature profiles compared with the boundary layer theory result, for $Pr = 0.72$.

where $f' = df/d\eta$. The temperature excess ratio remains defined as $\phi = (t - t_\infty)/(t_0 - t_\infty)$.

Figure 10(a) compares the calculated streamwise component, u, with boundary layer results, in terms of f', for $Pr = 0.72$. The difference in the numerically determined velocity profiles from boundary layer theory decreases downstream, as x increases. However, some difference does remain, even at large $x = 100$. This is due to the greater mass flow resulting from the increased entrainment from the region upstream of the leading edge. The induced horizontal entrainment flow, in Fig. 10(b), also shows increased agreement, for increasing x. Recall that the boundary layer formulation is not applicable outside the boundary layer region. It is merely the first term in an inner expansion of a perturbation solution of the full equations. However, the boundary layer formulation becomes increasingly more accurate adjacent to the surface and far downstream of the leading edge. Recall that the boundary layer solution does not include an entrainment flow from the region upstream of the leading edge. The result is that the boundary layer solution has a smaller u-component, in the absence of the leading edge entrainment. The numerical calculations show the effects of including the leading edge entrainment flow on the rest of the entrainment region.

The numerical results also show that v is outward from the surface, in the leading edge region, as seen in Fig. 10(b). This outward flow results from drag as it encounters and passes the leading edge of the bounding surface. The flow deflects away from the surface in this region, around the leading edge. This effect amounts to the displacement of the local maximum u-velocity away from the $y = 0$ axis, where it is for $x < 0$. The local maximum u-velocity moves to a position within the developing boundary layer, downstream of the leading edge. This trend continues only a short distance downstream of the leading edge. Thereafter, the v-direction flow, adjacent to the surface, reverses to that of coming towards the surface.

The temperature excess ratio is mediated by conduction, across the boundary region. As a result, there is less difference between the temperature excess ratio, ϕ, found by numerical calculation and the classical boundary layer theory. Figure 10(c) shows the comparison. However, the difference between the numerical and boundary layer theory temperature profiles decreases downstream.

4.5. *Maximum streamwise velocity, surface heat flux and surface shear stress*

The calculated local maximum vertical velocity, u, as a function of x, is compared with the results of boundary layer theory, for $Pr = 0.72$, in Fig. 11. Below the leading edge, the calculated maximum occurs at $y = 0$. Downstream of the leading edge, the local maximum u occurs within the downstream developing boundary layer. The boundary layer theory excludes any flow ahead of the leading edge. The maximum values of u tend toward the classical boundary layer result, in the downstream boundary layer. Numerical results are slightly higher than those predicted by boundary theory. This is again due to the inclusion of the leading edge entrainment flow in the new results.

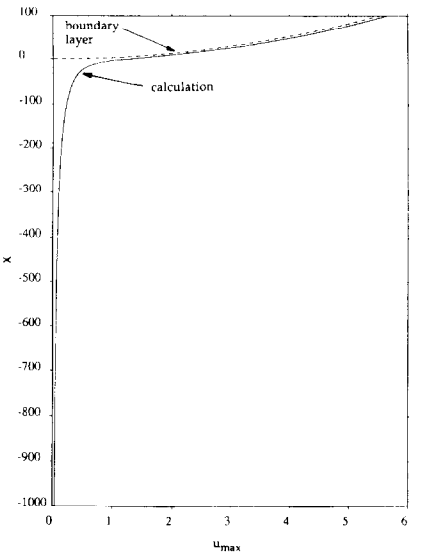

FIG. 11. Calculated local maximum streamwise velocity compared with the boundary layer results, at a given x, for $Pr = 0.72$.

Figure 12(a) compares the calculated wall heat flux with boundary layer behavior. As with the temperature excess profiles, the numerical calculations and boundary layer results agree closely. However, the numerical calculation show a finite value for the heat flux at the leading edge. Classical boundary layer theory is unbounded there. Recall Fig. 2(b). The upstream conduction effect, around the leading edge, leads to bounded temperature gradients over the whole field.

Figure 12(b) compares the computed surface shear stress, $\tau_w = \mu(\partial u/\partial y)$, with the boundary layer result. The downstream trends are similar. However, at the leading edge, boundary layer theory predicts a zero shear stress. This follows from $u = 0$, identically, at $x = 0$, as predicted by boundary layer theory. Recall equation (21). The boundary layer theory and numerical results diverge as the leading edge is approached. There the numerically calculated shear increases. At the leading edge, the gradients become very large, as the flow changes to accommodate the surface and the no-slip condition there, arising at $x = 0$. Similar results arise for the maximum u, the surface heat flux and the surface shear stress, for $Pr = 6.7$, as discussed in Wright [22].

4.6. *Motion pressure field*

The calculated motion pressure isobars, shown as dashed lines, and the streamlines, for $Pr = 0.72$, are

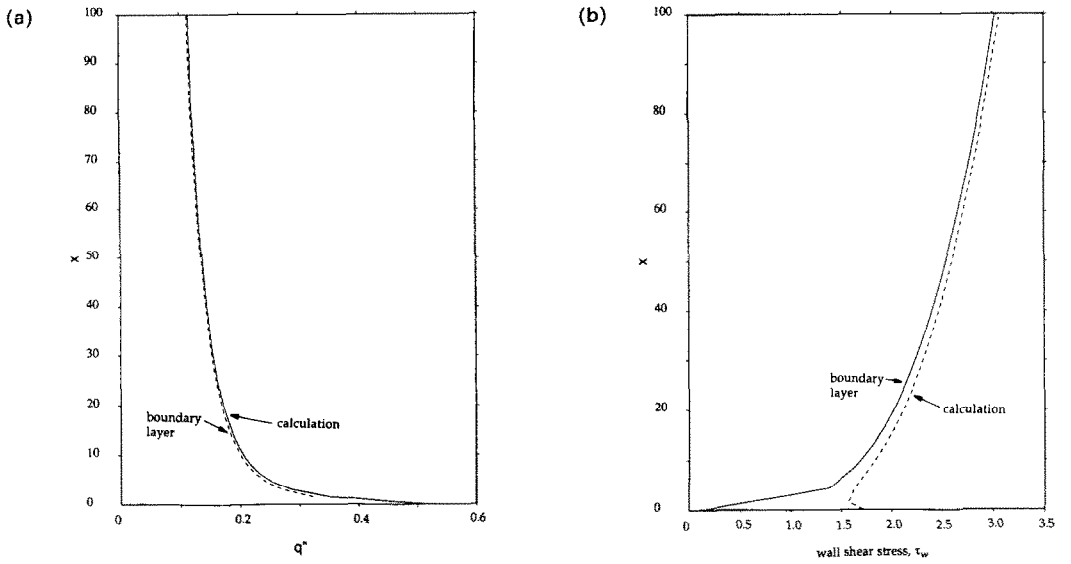

FIG. 12. (a) Calculated local surface heat flux compared with that from boundary layer theory, for $Pr = 0.72$; (b) calculated local wall shear stress compared with that from boundary layer theory, for $Pr = 0.72$.

shown in Fig. 13. All values of the isobars are negative. This arises because the motion pressure is the deficit from the distant ambient pressure, p_∞, owing to the combined effects of motion, viscosity and buoyancy. The largest magnitude of the motion pressure occurs near the leading edge. The value is $p = -0.5054$. The isobar $p = -0.05$ lies outside the boundary layer. It is little influenced by the effects of viscosity or buoyancy. It coincides with the dynamic pressure due to an inviscid entrainment flow. The calculated isobars contain some anomalies, very far from the surface. This arises at isobaric values that are less than 10% of the maximum calculated motion pressure. The error arises in calculating the pressure field from the streamfunction field. The streamfunction is an integration of the velocity. The result is that errors in the calculated velocity are smoothed when shown as streamlines. The pressure, however, is a differentiation of the velocity. This amplifies the effects, on the motion pressure, of errors in the numerically calculated velocity.

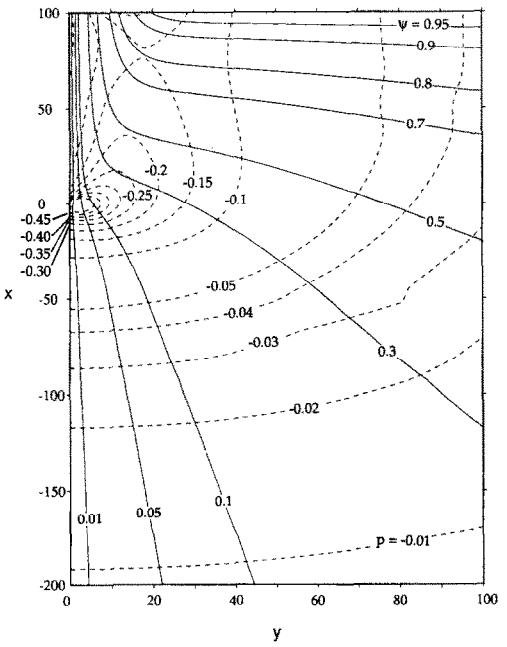

FIG. 13. Calculated streamlines and motion pressure isobars, for $Pr = 0.72$ and $Gr = 10^6$. Surface lies $0 \leqslant x \leqslant 100$.

The variation of p at $y = 0$, along the surface, is shown in Fig. 14. The greatest magnitude is near the leading edge. The immediate leading edge is a region of very large vorticity generation. The flow first encounters the surface and is retarded by the no-slip condition there. This vorticity generation causes the large increase in the magnitude of the motion pressure at this location.

5. CONCLUSIONS

The steady entrainment flow has been calculated for a vertical isothermal surface, $Gr_{max} = 10^6$, for fluids of $Pr = 0.72$ and $Pr = 6.7$. The physical coordinates were transformed to allow the boundary conditions to be specified far out from both the surface and its leading edge. A streamfunction–vorticity form of the Navier–Stokes equations was numerically integrated to calculate the velocity and the temperature fields. The Poisson equation for the motion pressure was integrated after these fields had been determined.

The entrainment flows found follow the trend suggested by previous perturbation analyses, for a semi-infinite vertical surface. Inclusion of the leading edge entrainment flow increases the boundary layer thick-

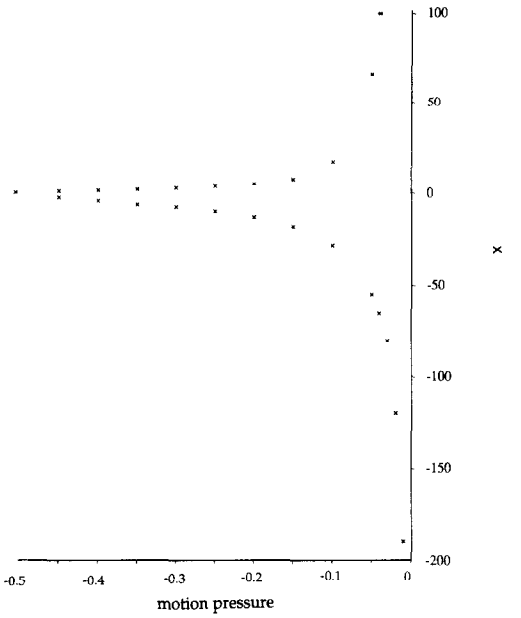

FIG. 14. Calculated motion pressure deficiency as a function of x, along $y = 0$, for $Pr = 0.72$. Surface lies $0 \leqslant x \leqslant 100$.

ness, immediately downstream of the leading edge of the surface. Further downstream, the boundary layer δ_n converges to approximately the boundary layer trend. The numerical calculation predicts a slightly greater δ_n, owing to the increased mass flow rate resulting from the included entrainment. The temperature boundary region thickness agrees well with the classical boundary layer results, downstream of the leading edge. The temperature field is largely determined by thermal conduction. It is insensitive to the small differences in the boundary region flow calculated here and by boundary layer theory. The numerical calculations show that conduction also plays a significant role in extending the temperature field upstream of the leading edge.

The agreement of the temperature and velocity profiles with classical boundary layer theory is increasingly close, downstream of the leading edge. Near the leading edge, the streamwise velocity is greater than the boundary layer result. The heat flux and shear stress, along the surface, closely follow the trend of boundary layer theory. The calculated maximum streamwise velocity is greater, owing to the higher leading edge entrainment flow. The motion pressure field due to the buoyancy-induced flow adjacent to the surface, drives this entrainment flow. The motion pressure deficit is greatest at the surface leading edge. This results in the leading edge region acting as a mass sink, for both the upstream and the lateral entrainment flows.

Acknowledgements—This work was supported by the National Science Foundation Grant CTS-8913393. This research was conducted using the Cornell National Supercomputer Facility.

REFERENCES

1. B. Gebhart, Y. Jaluria, R. Mahajan and B. Sammakia, *Buoyancy-Induced Flows and Transport*. Hemisphere, New York (1988).
2. E. Schmidt and W. Beckmann, Das Temperatur und Geschwendigkeitsfeld vor einer Wärme abgebenden senkrechten Platte bei natürlicher Convection, *Technische Mechanik und Thermodynamik* **1**, 341–349, 391 406 (1930).
3. L. Prandtl, Über Flüssigkeitsbewegung bei sehr kleiner Reibung, *Proceedings of the Third International Mathematics Congress*, Heidelberg, pp. 484–491 (1904).
4. H. Schuh, Temperature boundary layers. In *Boundary Layers* (Edited by W. Tollmein), Sec. B6. British Ministry of Supply, German Doc. Cent. Ref. 3220T (1948).
5. S. Ostrach, An analysis of laminar free-convection flow and heat transfer about a flat plate parallel to the direction of the generating body force, NASA TR 1111 (1953).
6. E. J. LeFevre, Laminar free convection from a vertical plane surface, *Actes IXe Cong. Int. de Mech. Appliquee* **4**, 168–174 (1957).
7. P. R. Nachtsheim and P. Swigart, Satisfaction of asymptotic boundary conditions in numerical solution of systems of nonlinear equations of boundary-layer type, NASA TN D-3004 (1964).
8. S. Sugawara and I. Michiyoshi, The heat transfer by natural convection in the unsteady state on a vertical flat wall, *Proceedings of the First Japanese National Congress for Theoretical and Applied Mechanics*, pp. 501–506 (1952).
9. K. T. Yang and E. W. Jerger, First-order perturbations of laminar free-convection boundary layers on a vertical plate, *ASME J. Heat Transfer* **86**, 107–115 (1964).
10. V. Kadambi, Singular perturbations in free convection, *Wärme- und Stoffübertragung* **2**, 99–104 (1969).
11. C. A. Hieber, Natural convection around a semi-infinite vertical plate: higher order effects, *Int. J. Heat Mass Transfer* **17**, 785–791 (1974).
12. I. Imai, *J. Aerospace Sci.* **24**, 155 (1958).
13. Y. Jaluria, Interaction of natural convection wakes arising from thermal sources on a vertical surface, *ASME J. Heat Transfer* **107**, 833–892 (1985).
14. L. Pera and B. Gebhart, Laminar plume interactions, *J. Fluid Mech.* **68**, 259–271 (1975).
15. R. Agarwal and Y. Jaluria, Deflection of a two-dimension natural convection wake due to the presence of a vertical surface in close proximity, *J. Fluid Mech.* **201**, 35–56 (1989).
16. Y. Joshi and B. Gebhart, Transition of transient vertical natural-convection flows in water, *J. Fluid Mech.* **179**, 407–438 (1987).
17. Y. Joshi and B. Gebhart, Transient response of a steady vertical flow subject to a change in surface heating rate, *Int. J. Heat Mass Transfer* **31**, 742–747 (1988).
18. N. Riley, Free convection from a horizontal line source of heat, *J. Appl. Math. Phys.* **25**, 817–828 (1974).
19. M. Afrid and A. Zebib, Natural convection air cooling of heated components mounted on a vertical wall, *Numer. Heat Transfer A* **15**, 243 259 (1989).
20. D. H. Pelletier, J. N. Reddy and J. A. Schetz, Some recent developments and trends in finite element computation natural convection. In *Annual Review of Numerical Fluid Mechanics and Heat Transfer* (Edited by C. L. Tien and T. C. Chawla), Vol. 2, pp. 39–85 (1989).
21. P. Roache, *Computational Fluid Dynamics*. Hermosa (1972).
22. N. T. Wright, Enhanced boiling heat transfer from microconfigured silicon surfaces and entrainment flow

adjacent to an isothermal vertical surface, Ph.D. Thesis, University of Pennsylvania, Philadelphia, Pennsylvania (1992).
23. J. A. Sills, Transformation for infinite regions and their application to flow problems, *AIAA J.* **7**(1), 117–123 (1969).
24. N. Riley, The heat transfer from a sphere in free convective flow, *Comput. Fluids* **14,** 225–237 (1986).
25. J. F. Thompson, Z. U. A. Warsi and C. W. Mastin, *Numerical Grid Generation, Foundations and Applications*. North-Holland, Amsterdam (1985).